Yuan Ma, Dawid Zimnik, Michael Dreyer, Yanzhong Li

Investigation on cryo-wicking performance within metallic weaves under superheated conditions for screen channel liquid acquisition devices (LADs)

Yuan Ma, Dawid Zimnik, Michael Dreyer, Yanzhong Li,
Investigation on cryo-wicking performance within metallic weaves under superheated conditions for screen channel liquid acquisition devices (LADs),
International Journal of Heat and Mass Transfer, Volume 141, 2019, Pages 530-541, ISSN 0017-9310,
https://doi.org/10.1016/j.ijheatmasstransfer.2019.06.103

Investigation on cryo-wicking performance within metallic weaves under superheated conditions for screen channel liquid acquisition devices (LADs)

Yuan Ma [a], Dawid Zimnik [b], Michael Dreyer [b], Yanzhong Li [a,c,*]

[a] Institute of Refrigeration and Cryogenic Engineering, Xi'an Jiaotong University, Xi'an 710049, China
[b] University of Bremen, Faculty of Production Engineering - Mechanical Engineering and Process Engineering, Department of Fluid Mechanics, ZARM, Am Fallturm 2, 28359, Germany
[c] State Key Laboratory of Technologies in Space Cryogenic Propellants, Beijing 100028, China

ARTICLE INFO

Article history:
Received 27 May 2019
Received in revised form 28 June 2019
Accepted 28 June 2019
Available online 4 July 2019

Keywords:
Liquid acquisition device (LAD)
Porous screen
Wicking
Cryogenic liquid
Evaporation

ABSTRACT

In order to investigate the wicking performance of cryogenic propellants within metallic screens for space liquid acquisition devices (LADs), a vertical wicking experiment was carried out in a one-species test system with liquid nitrogen (LN_2). Screens of Dutch twill weave (DTW) type 200 × 1400 were tested in both warp and shute directions. Two different degrees of superheat (~2 K and ~25 K) were achieved with a novel porous cooling shield element. A modified one-dimensional macroscopic model is proposed which considers the thermal effect of the solid weave and the vapor environment. Good agreement with experimental data is achieved. Results show that the cryo-wicking process is sensitive to the superheat condition. The wicking velocity as well as the maximum wicking height decreases with increasing superheat. For the same superheat condition, the wicking velocity was always higher in the warp direction than that in the shute direction.

1. Introduction

Gas free delivery of liquid propellants is of great necessity for the safety and reliability of engine operations or other propellant transportation requirements. The liquid-gas distribution in reduced gravity environments depends on many parameters. Propellant management technologies must be applied for space flight missions in order to guarantee the gas free liquid delivery of propellants [1,2]. Owing to the high thrust and nontoxicity, cryogenic propellants such as liquid hydrogen, liquid methane and liquid oxygen, are considered as an ideal option for future deep space missions [3]. However, special physical properties of cryogenic propellants including low boiling point, low viscosity and low surface tension, also brings new challenges to the orbital propellant management technology [4–6]. Compared with several feasible methods, the screen channel liquid acquisition devices (LADs), whose orbital availability of single phase liquid delivery has been successfully verified for storable fluids, is considered the most robust and applicable option for cryogenic propellants [7–10]. Fig. 1 shows the schematic of a typical screen channel LAD with four full communication channels. Within the tank, channels are uniformly installed in each quadrant and are joined together at the outlet. On the side facing the inner tank wall, each channel is covered with a piece of porous screen. This screen is woven with metallic wires and has microscopic openings that could imbibe liquid into the channel but block the gas ingestion depending on the surface tension and capillary forces [11].

The mechanism of phase separation and detailed operation performance of this screen channel LAD has been studied for several decades, and from 1990s, increasing attention has been payed upon cryogenic liquids. The bubble point pressure, representing the gas blocking capacity of the porous screen, has been deeply analyzed and tested in several cryogenic liquids [12–17]. Meanwhile, as an indication of the gas free liquid outflow characteristics, the pressure drop of LAD channels has also been comprehensively studied through theoretical, numerical and experimental methods [18–20].

Besides, the liquid wicking phenomena within the screen is regarded as the critical foundation of the LAD operation since the gas blocking function is only available after the porous screen is saturated with liquid [21,22]. If the screen is partially dry, wicking could also provide a degree of self-repairing for saturation recovery [23]. Liquid transport processes driven by capillary force inside porous media are generally called "wicking", the ones with

* Corresponding author at: Institute of Refrigeration and Cryogenic Engineering, Xi'an Jiaotong University, Xi'an 710049, China.
E-mail address: yzli-epe@mail.xjtu.edu.cn (Y. Li).

https://doi.org/ 10.1 01 6/j.ijheatmasstransfer.2019.06.

Nomenclature

Latin letters

A	surface area/m^2
C	empirical coefficient
c	specific heat capacity/J kg^{-1} K^{-1}
c_p	specific heat capacity at constant pressure/J kg^{-1} K^{-1}
D	wire diameter/m
D_c	equivalent capillary diameter/m
Gr	Grashof number
g	gravity/m s^{-2}
H	height of sample/m
h	wicking height/m
h_{fg}	latent heat of evaporation/J kg^{-1}
K	permeability/m^2
k	coefficient of heat transfer/W K^{-1} m^{-2}
q	heat exchange capacity/J
$\dot{q}$	heat transfer rate/W
l	characteristic length/m
m	mass/kg
Nu	Nusselt number
N	empirical coefficient
Pr	Prandtl number
T	temperature/K
t	time/s
u	wicking velocity/m s^{-1}
W	width/m

Greek letters

α_v	expansion coefficient/K^{-1}
ΔT	temperature difference/K
δ	thickness/m
θ	contact angle/°
λ	thermal conductivity/W m^{-1} K^{-1}
μ	dynamic viscosity/Pa s
ν	kinematic viscosity/m^2 s^{-1}
∇T	vertical temperature gradient/K m^{-1}
ρ	density/kg m^{-3}
σ	surface tension/N m^{-1}
ϕ	porosity/–

Subscripts

0	initial state
e	evaporation
g	gas
l	liquid
max	maximum
S	shute
s	solid
W	warp

Abbreviation

DTW	Dutch twill weave
LAD	liquid acquisition device
LSH	low superheat
HSH	high superheat

cryogenic liquids are usually called "cryo-wicking" [24]. Symons [25] tested the wicking performance of 13 different metallic screens under normal and micro gravities, with methanol and ethanol as test liquids. Dodge et al. [26] investigated the vertical and horizontal wicking performance of several screens in isopropyl alcohol. Fries et al. [23] conducted a vertical wicking experiment in five storable liquids using 200 × 1400 Dutch twill weave (DTW) and investigated the effects of evaporation. Subsequently, Conrath et al. [27], Hartwig and Darr [28] also experimentally investigated the wicking process within several metallic weaves using storable liquids. Ma et al. [29] recently conducted an isothermal vertical experiment in HFE-7500 to measurement the structural parameters of three DTWs. Meanwhile, Conrath et al. [30] studied the horizontal inward and outward radial wicking process within filter papers and established a theoretical model based on Darcy's law. Zhang et al. [31], Shirazy and Fréchette [32] experimentally investigated the capillary wicking and wetting performance of copper metal foams. Liu et al. [33] performed water wicking experiment within fibrous paper and modified the Lucas-Washburn model by adding the evaporation effect caused by humidity difference. However, according to the existing literatures, researches regarding to cryo-wicking are still very limited. Hastings et al. [34] experimentally investigated the wicking process of liquid nitrogen into metallic weaves, but no detailed data were presented. Zhang et al. [35] comparatively studied the wicking and heat transfer performance of liquid nitrogen within a multi-layer metallic wire cloth laminate, and indicated the metallic meshes screen with strong wicking was an efficient porous structure for fluid and thermal management in space. Choi et al. [36] conducted an experimental investigation on the flow phenomenon of liquid nitrogen in porous glass wool. The permeability was measured and it was affected by the applied pressure and bulk density. Grebenyuk et al. [37] tested the wicking velocity of liquid nitrogen into the porous glass frit samples by mass measurement method, and theoretically analyzed the effects of superheat degree.

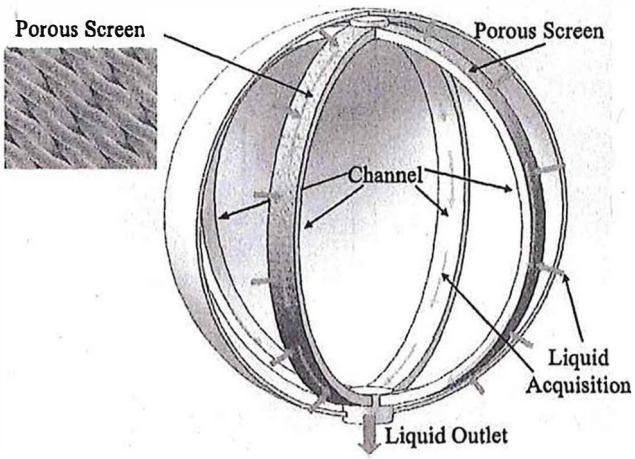

Fig. 1. Schematic diagram of a screen channel liquid acquisition device.

From the above, although wicking has direct effects on both obtaining and maintaining a screen channel LAD for orbital propellant management, studies concerning cryo-wicking and the evaporation effects on wicking performance are still extremely deficient. In this paper, the vertical wicking of saturated liquid nitrogen at atmospheric pressure was experimentally investigated through an imbibition mass measurement method. The non-isothermal wicking performance was tested within DTW 200 × 1400 in both warp and shute directions under two different superheat degrees. Besides, the standard porous-continuum model was modified to take the evaporation effects caused by superheating the screen and the vapor environment into account.

2. Theory

Wicking in porous media has been theoretically studied through many different methods [38,39]. The porous-continuum model has proven to be an appropriate model for woven screens with a regular and uniform porous structure, such as the DTWs used in this study. Isothermal wicking can be predicted with a good accuracy [23,27,28]. In this model, the porous medium is hypothesized to be uniform with constant structural parameters, and is simplified into a bundle of straight capillary tubes of the same diameter [23,29,38]. After an initial contact with a liquid surface, the liquid would initially wick into the capillary under the strength of capillary pressure, and be resisted by the viscous and hydrostatic force. In case of a vertical orientation of the main axis of the screen, the balance equation of linear momentum takes the form

$$\frac{4\sigma\cos\theta}{D_c} = \frac{\phi\mu_l h u}{K} + \rho_l g h. \tag{1}$$

With the initial condition $h\,(t=0)=0$, the relationship between time t and the height of isothermal wicking front h could be solved into

$$t(h) = -\frac{\phi\mu_l}{\rho_l g K}h - \frac{4\sigma\cos\theta\phi\mu_l}{D_c\rho_l^2 g^2 K}\ln\left(1-\frac{D_c\rho_l g}{4\sigma\cos\theta}h\right). \tag{2}$$

As shown in Fig. 2, a meniscus appears at the outside of the screen due to the capillary effects as well. Therefore, the surface of the liquid contacting the screen surface, namely the upper edge of the submerged part of the screen, exceeds a height of the meniscus compared with the free surface of the liquid bath. In order to calculate the development of the real wicking height, the origin is located at the top of the meniscus. Meanwhile, this model depends on a persistent contact between the screen bottom and the liquid bath to guarantee the continuous replenishment of liquid for the wicking process.

The wicking front is assumed as a sharp interface between the fully saturated region below and a fully dry region above [38]. With the effect of gravity, vertical wicking has a maximum reachable height when the hydrostatic pressure of this liquid column is balanced by the capillary pressure. The maximum height is calculable as

$$h_{max} = \frac{4\sigma\cos\theta}{\rho_l g D_c}. \tag{3}$$

Based on this isothermal model, Fries et al. [23] proposed a modified model to predict the effect of evaporation on the wicking of storable liquids. This model requires the evaporation rate from experimental measurement as an input value. Grebenyuk et al. [37] also enhanced the isothermal model to evaluate the thermal effect of a superheated porous structure, but they neglected the thermal energy exchange with the surrounding gas. In this paper, a modified model based on the porous-continuum method is proposed where both the thermal effects of the solid and the gas regions are considered.

2.1. Governing equations

For the evaporative wicking process as shown in Fig. 3, the momentum balance at the bottom inlet should be equal to Eq. (1), but states differently at the wicking liquid front as

$$\frac{4\sigma\cos\theta}{D_c} = \frac{\phi\mu_l h u_e}{K} + \rho_l g h + p_e. \tag{4}$$

The effect of liquid evaporation p_e causes the interface velocity u_e to be different from the inlet velocity u. They are equal for the isothermal case. This difference can be related by a mass balance of

$$(u-u_e)\delta W\phi\rho_l = \frac{dm_e}{dt}. \tag{5}$$

It is assumed that the heat for cooling is taken from the latent heat of evaporation for a saturated liquid. Two terms of evaporated liquid mass are considered here, one is due to the evaporation at the wicking front, caused by the heat transfer from the superheated solid, and one is due to the evaporation at the sides of the saturated sample, caused by heat transfer from the superheated gas region. Therefore, the latent heat of the evaporative mass flow should be equal to the heat transferred from the superheated solid structure and the superheated vapor. The energy balance can be express as

$$\frac{dm_e}{dt}h_{fg} = \frac{dq_{sl}}{dt} + \frac{dq_{gl}}{dt}. \tag{6}$$

Therefore, coupling Eqs. (5) and (6), unknown parameter u_e could be obtained, finally the development of the evaporative wicking height $h(t)$ can be calculated by Eq. (4).

Due to the high specific surface area of the porous screen, the heat transfer between cold liquid and superheated solid screen is not negligible. The solid structure is supposed to be cooled down instantaneously from its initial temperature T_s to the liquid

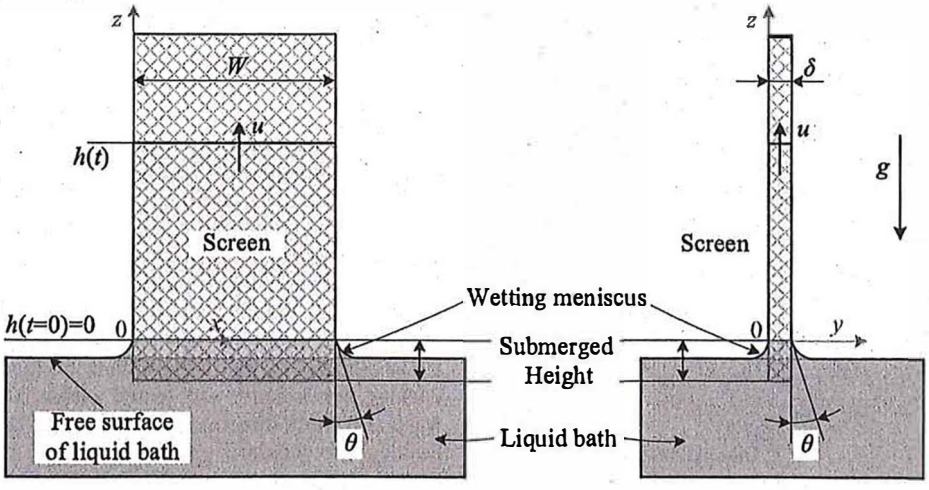

Fig. 2. Schematic diagram of the wicking phenomenon in a porous screen.

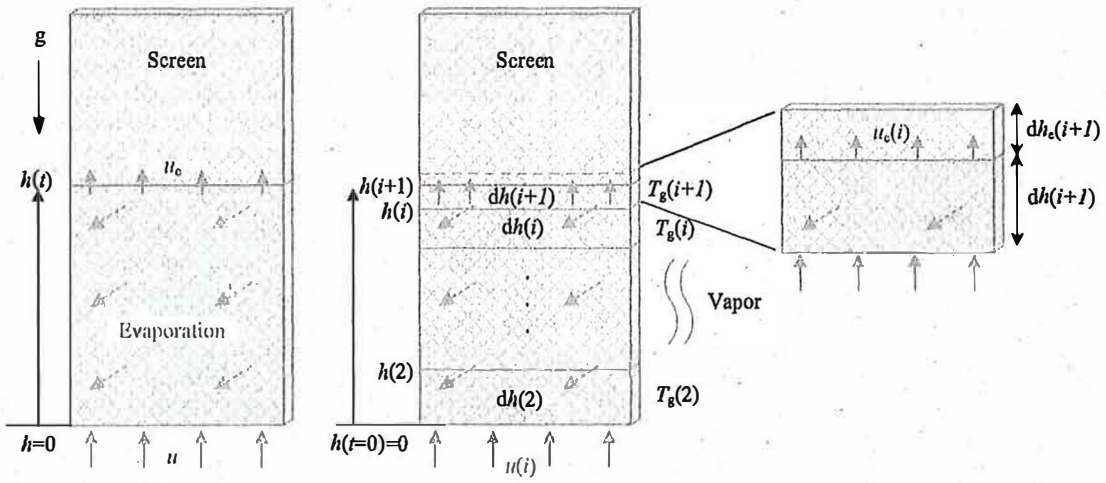

Fig. 3. Schematic diagram of the evaporation-modified wicking model.

temperature T_l. Therefore, when u_e is given, the mass of the solid part which would be wetted by the wicking liquid, m_s, can be obtained, and then the heat flux from solid to liquid can be calculated by

$$\frac{dq_{sl}}{dt} = \frac{m_s c_s (T_s - T_l)}{dt} = u_e \delta W (1-\phi)\rho_s c_s (T_s - T_l). \tag{7}$$

In this model, the gas region is supposed to be big enough with constant temperature. The initial temperature distribution of the solid screen is assumed to be the same as in the surrounding gas, and the heat conduction in the solid is neglected. The dry screen above the wicking front always has the same temperature with the contacting gas region, where no heat transfer occurs. Meanwhile, the wet screen part below the wicking front is at the saturation temperature of the liquid. The temperature difference between the wet screen and the surrounding superheated gas will induce heat transfer and the evaporation of the imbibed liquid.

In view of the relatively smooth surface of the saturated porous screen and the slow wicking velocity, the heat transfer between the wet screen and the surrounding gas is assumed as a natural convection issue from vertical plates [40]. The heat transfer coefficient could be obtained by the correlations of

$$k = Nu \frac{\lambda_g}{l}, \tag{8}$$

and the heat flux from gas to the wet screen surface can be expressed as

$$\frac{dq_{gl}}{dt} = kA\Delta T = 2k(\delta + W)h(T_g - T_l). \tag{9}$$

Nu can be expressed in the form

$$Nu = C(Gr \cdot Pr)^n, \tag{10}$$

where

$$Gr = \frac{gl^3 \alpha_{vg} \Delta T}{\upsilon_g^2}, \tag{11}$$

$$Pr = \frac{\mu_g c_{pg}}{\lambda_g}. \tag{12}$$

ΔT is defined as the temperature difference between the gas region and the saturated liquid. The wicking height h is taken as the characteristic length l of Gr [42]. In the range $1.43 \times 10^4 \le Gr < 3 \times 10^9$, the empirical coefficients $C = 0.59$ and $n = 0.25$ apply; in the range $3 \times 10^9 \le Gr < 2 \times 10^{10}$, $C = 0.0292$ and $n = 0.39$ apply; for $Gr \ge 2 \times 10^{10}$, the values are $C = 0.11$ and $n = 1/3$ [41]. When the value of the Grashof number is lower than 1.43×10^4, taking no account for heat transfer by conduction or radiation, the thermal effect of the gas region is assumed to be negligible and the heat transfer coefficient of the natural convection is assumed to be zero in this model.

2.2. Solving algorithm

To solve this evaporative wicking problem, the wicking process is discretized in time and the wicking height can be accordingly divided into several slices. Fig. 3 also gives an illustration of the modeling process, where symbol i represents the number of the time step. At the initial time $t(1) = 0$ s, the sample bottom just contacts the liquid surface and the wicking height $h(1)$ is zero. At an arbitrary time $t(i)$, the increase of the evaporative wicking height during the next time step is

$$dh(i+1) = u_e(i)dt. \tag{13}$$

The wicking height change due to the evaporated liquid can be calculated as

$$dh_e(i+1) = u(i)dt - u_e(i)dt = \frac{m_e(i+1)}{\delta W \phi \rho_l}. \tag{14}$$

Referring to Eq. (6), the evaporated liquid mass in this time step consists of two terms

$$m_e(i+1) = \frac{q_{sl}(i+1) + q_{gl}(i+1)}{h_{fg}}, \tag{15}$$

one is due to the evaporation at the wicking front, caused by the heat transfer from the superheated solid, and one is due to the evaporation at the sides of the saturated sample, caused by heat transfer from the superheated gas region.

In this model, the solid, liquid and gas regions are all divided into several slices matching with the wicking height development. The lumped parameter method is adopted for all slices, which means each slice can be treated as a single point with uniform physical properties. Therefore, the heat transferred from solid to liquid in this time step equals to the internal energy change of the solid part in $dh(i+1)$, which can be calculated by

$$q_{sl}(i+1) = dh(i+1)\delta W(1-\phi)\rho_s c_s (T_s(i+1) - T_l). \tag{16}$$

The total heat transfer from gas to the wet screen surface during one time step is

$$q_{gl}(i+1) = \sum_{j=1}^{i+1} k_j \cdot 2(\delta + W)dh(j) \cdot (T_g(j) - T_l) \cdot dt. \tag{17}$$

If there is a linear temperature gradient along the screen height, the local temperatures of the gas region are defined by this temperature gradient and the initial temperature T_0 at the sample bottom as

$$T_g(i+1) = T_{0g} + \nabla T\left(h(i) + \frac{1}{2}dh(i+1)\right). \quad (18)$$

The same method is used for the solid screen with linear temperature distribution.

3. Experiments

3.1. Experiment arrangement

The apparatus of the cryogenic wicking experiment is depicted in Fig. 4. The cryostat (manufacturer Cryovac, Germany) is made of stainless steel with an outer diameter of 394 mm and an overall height of 725 mm. A flange with a diameter of 360 mm and a thickness of 15 mm is welded on the top of the container and is connected to an inner cylinder with a diameter of 296 mm and a maximum inner height of 602 mm. The lower inner bottom of the container has an ellipsoid shape with a height of 45 mm. The container has a volume of 43 L and can be closed with a top lid (diameter 360 mm, thickness 13 mm). The volume between the inner and the outer cylinders is evacuated to a pressure below 1.3×10^{-3} Pa.

The coordinate system is fixed to the uppermost edge of the container (without the sealing flange). A baffle made of stainless steel (diameter 290 mm, thickness 1 mm) is placed at $z = -465$ mm. It has an opening in the center to move the sample into the lower part and other openings for the temperature measurement rod, gas/liquid pipes, endoscope, etc. The aim of the baffle is to thermally separate the electronic elements located above from the lower cryogenic environment. The inner side of the top plate is at several degrees below outside ambient temperature, depending on the particular experiment conditions. The lower part of the inner cylinder is filled with liquid nitrogen to a level which is always below the baffle. The wall of the inner container below the baffle is covered with a piece of DTW 325 × 2300 (thickness 90 μm, provided by SPÖRL, Germany) around its circumference. The mesh extends from −465 mm to −565 mm. If the level of liquid nitrogen is within this range, the mesh is saturated with liquid nitrogen and provides a thermal boundary condition. If the liquid level decreases below the lower range, the mesh would dry out and the wall temperature would increase. This effect can be used to thermally control the lower part of the container.

A movable platform is connected to the top lid with three threaded bars and three stepper motors (L3518S1204-T6x1, Nano-Tec, Germany). A high-precision electronic balance (WZA-224, Sartorius, Germany) with an accuracy of ±0.1 mg is positioned in the center of the platform. A sample holder hangs freely below the balance by a metal wire of 200 mm length and 2.8 mm diameter. The sample hold can clamp the screen sample and protrude through the baffle into the lower part of the cryostat. As shown in Fig. 5, there is an obtuse angle between two splints of the sample holder, which does not keep the sample completely flat but imposes a certain shape on the sample. This slight circumferential bending of the sample can effectively avoid undesirable curling in the vertical direction. Through the remote control of the stepper motors by a computer, the position of the platform, namely the distance between sample bottom and liquid surface can be adjusted with a velocity of 1 mm s^{-1} and a minimum step of 1 mm.

A temperature measurement rod (11 in Fig. 4) vertically extends from the top lid towards the bottom of the cryostat, as the rod 1 shown in Fig. 5. This rod consists of an epoxy glass plate with scale (length 660 mm, width 22.5 mm, thickness 3 mm) and ten temperature sensors (T_1-T_{10}) allocated along its length. A

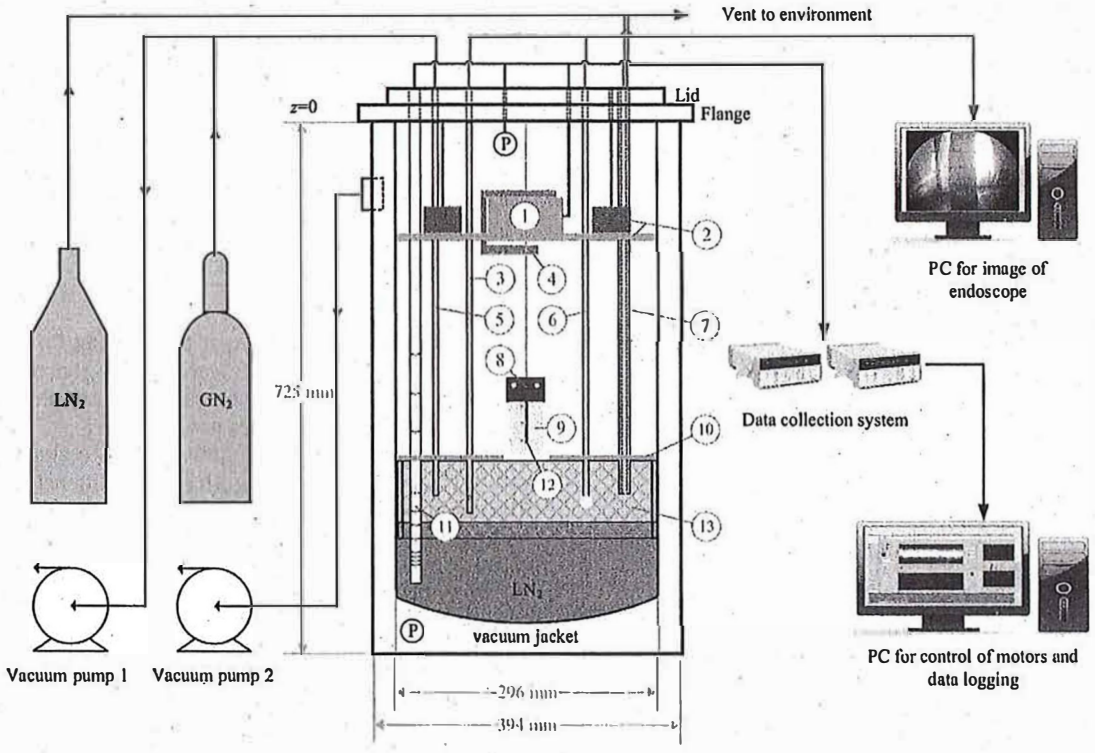

Fig. 4. Sketch of the experiment arrangement. 1. Weighing cell; 2. Height changeable platform; 3. Endoscope; 4. Free-hanging frame; 5. GN_2 filling/vacuum pumping pipe; 6. Illumination; 7. LN_2 filling pipe (inner)/vent pipe (outer); 8. Sample holder; 9. Test sample; 10. Baffle; 11. Temperature rod 1 fixed to the top lid; 12. Temperature rod 2 fixed to the sample holder; 13. Porous cooling shield.

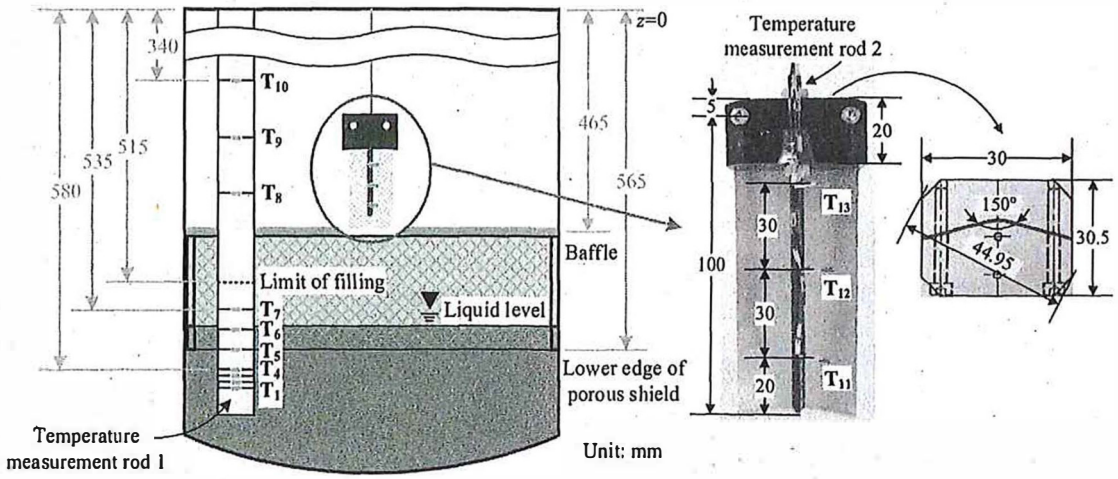

Fig. 5. Locations of two temperature measurement rods.

smaller temperature measurement rod (12 in Fig. 4) made of polyacetal (length 80 mm, diameter 4 mm) is installed on the sample holder. Three temperature sensors (T_{11}-T_{13}) are allocated along its length. The data monitoring and recording were programmed with LabVIEW.

3.1.1. Measurement devices

The main idea to obtain the wicking process is measuring the mass development of the imbibed liquid within the porous sample. The pressure inside the cryostat is measured with a pressure sensor (TJE-1256-30, Sensotec, Germany) with an accuracy of ±0.2 kPa.

Temperature are measured by 13 temperature sensors (DT-670A, LakeShore, America) with an accuracy of ±0.25 K at temperatures from 2 K to 100 K and ±0.5 K at temperatures from 100 K to 305 K. 10 sensors (T_1-T_{10}) are mounted on rod 1. $T_{8\text{-}10}$ are located above the baffle with an equal spacing of 45 mm, while others are below the baffle with an equal spacing of 15 mm for T_4-T_7 and 5 mm for T_1-T_4. This measurement technique has already been used by Grebenyuk et al. [37]. The aim of this device is to measure the temperature distribution in the cryostat at fixed locations. The locations of the sensors are given in Table 1.

The rest three sensors (T_{11}-T_{13}) are attached to rod 2 without contacting the sample. This rod can synchronously move with the sample to measure the temperature of the gas in the vicinity of the sample at different positions fixed to the sample holder. The sensors are supposed to be in the gas phase all the time. The distances of the sensors from the bottom of the screen are 20 mm for T_{11}, 50 mm for T_{12} and 80 mm for T_{13}, which are also given in Fig. 5.

Table 1
Location of the temperature sensors on temperature measurement rod 1.

Number	z/mm	Comment
1	−595	Liquid or gas
2	−590	Liquid or gas
3	−585	Liquid or gas
4	−580	Liquid or gas
5	−565	Liquid or gas
6	−550	Liquid or gas
7	−535	Liquid or gas
8	−430	Gas
9	−385	Gas
10	−340	Gas

*The coordinate system is fixed to the uppermost edge of the container (without the sealing flange). The comment column indicates in which phase the sensors are intended to measure the temperature.

3.1.2. Optical means

The lower part of the cryostat can be visually inspected with an endoscope. The position of the lens can be adjusted. The endoscope is connected to a camera (CCT-1/4″ Chip). Fig. 6 shows two images from the lower part of the cryostat. Two temperature measurement rods and the screen sample can be observed clearly. The porous screen at the wall can be seen in the background. The liquid level is clearly visible.

3.2. Screen samples and test fluid

Two samples of DTW 200 × 1400 (made of stainless steel AISI 304 L) were cut, one in warp direction and one in shute direction (sometimes called weft direction as well). The warp direction means wicking is parallel to the warp wires. The samples are aligned with the warp direction parallel to the gravity vector, or with the shute direction. The related information of each sample is listed in Table 2. The height and width were measured by an optical microscope (Kiestrel Wision Dynascope K 07546, Leybold). The heights of the two samples are about 100 mm. Considering the part clamped in the sample holder with a height of 15 mm (Fig. 5), the free length of the samples is about 85 mm. The thermophysical properties of the solid material were obtained from Material Properties DataBase (MPDB), other information was provided by the supplier (SPÖRL, Germany).

Referring to Section 2, macroscopic parameters including porosity, equivalent capillary diameter and permeability are also important parameters for screens. Due to the difficulty of achieving the isothermal environment in cryogenic LN_2, these three parameters were not directly measured in this experiment. The measurement results of the same samples from an isothermal wicking experiment in storable liquid (HFE-7500) were used. The corresponding data are listed in Table 3 [29]. In theory, these structural parameters should be constant for a certain porous structure even in different fluids [23,37]. However, from the comparison among the history data in Ref. [29], the existing results of these parameters might be still divergent and discrepant.

The wicking experiment was carried out in saturated LN_2 at normal pressure conditions. The static contact angle between LN_2 and the stainless steel is assumed to be zero [37], other properties were obtained from NIST REFPROP and are listed in Table 4.

3.3. Experiment procedures

At the beginning of the experiment campaign, the cryostat was filled with gaseous nitrogen to replace the air. The cryostat was

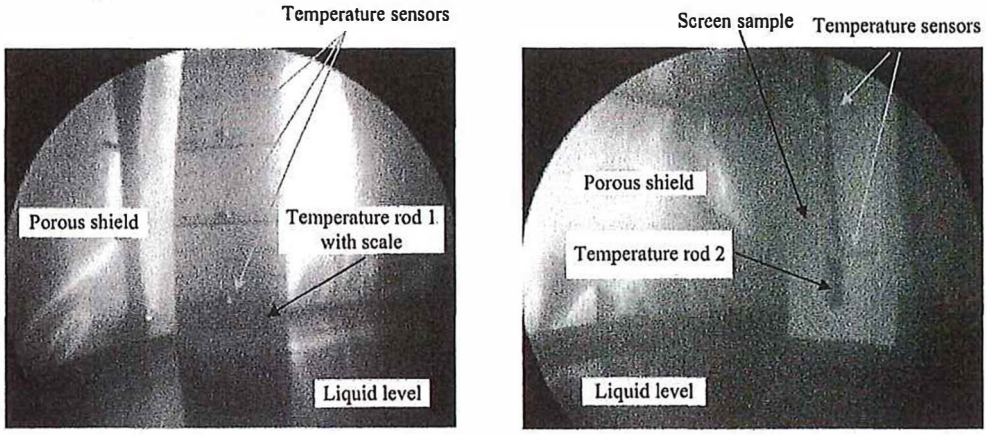

Fig. 6. Views obtained from the endoscope.

Table 2
Information about the test samples.

Direction	H/mm	W/mm	δ/μm	D_W/μm	D_S/μm	ρ_s/kg m^{-3}		c_s/J kg^{-1} K^{-1}		λ_s/W m^{-1} K^{-1}	
						77 K	120 K	77 K	120 K	77 K	120 K
Warp	99.68	38.81	150	70	40	7930		204.62	317.31	7.92	10.10
Shute	99.80	39.87									

Table 3
Measurement and fitting results of macroscopic parameters in Ref. [29].

Parameter	ϕ/–	D_{cw}/μm	K_W/μm^2	D_{cs}/μm	K_S/μm^2
Average	0.254 ± 0.013	43.26 ± 0.41	1.165 ± 0.015	47.58 ± 0.17	0.544 ± 0.007

Table 4
Thermo-physical properties of saturated nitrogen at 101,325 Pa and 77.355 K [37].

Phase	ρ/kg m^{-3}	μ/μPa s	ν/mm^2 s^{-1}	λ/mW m^{-1} K^{-1}	c_p/kJ kg^{-1} K^{-1}	α_v/mK^{-1}	σ/mN m^{-1}	h_{fg}/kJ kg^{-1}
Liquid	806.08	160.66	0.20	144.77	2.04	–	8.87	199.18
Gas	4.61	5.44	1.18	7.19	1.12	14.74	–	–

evacuate by a vacuum pump (Drehschieber) to a pressure below 3 kPa, and then flushed with gaseous nitrogen. This procedure was repeated three times. After that, the cryostat was filled with liquid nitrogen with an open connection to ambient pressure. A refill was required after about 5 h. A steady temperature distribution was achieved after 10 h, as depicted in Fig. 7-left. When the liquid level dropped below the position of sensor T_7, an increase of temperature was recorded at 13.3 h after the start of the chill down procedure (see Fig. 7-right). The same happened when the liquid level dropped below the position of sensor T_6 at 14.5 h. After the detachment from the liquid level, the temperatures of T_7 and T_6 stayed below 78 K, indicating a low superheat of the vapor of around 1 K. This condition remained for another 7 h, before the sensor T_5 detached from the liquid surface. This sensor is at the same level as the screen which covers the side walls of the cryostat. As long as the screen stays in contact with liquid nitrogen, it

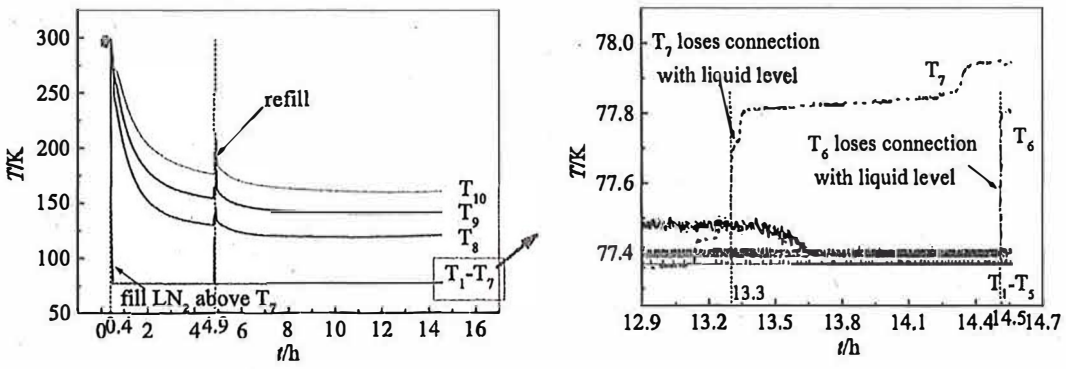

Fig. 7. Stable process for establishment of low superheat condition.

remains saturated and provides a constant temperature condition below the baffle. This condition was used as an initial condition to bring the test sample to the same temperature as the vapor. It is named as low superheat condition, or LSH.

When the liquid level dropped below $z = -565$ mm, i.e. the lower edge of the screen shield and the position of sensor T_5, the temperatures in the cryostat started to rise. As shown in Fig. 8, a temperature stratification was built up. It can be observed that this temperature stratification remained fairly constant when the liquid level reached sensor T_4. This condition was used as an initial condition for the wicking tests, referred to as high superheat condition, or HSH. The rate of decrease of the free surface was approximately 20 min mm^{-1}, and therefore giving sufficient time to perform three measurements when the liquid level was between T_4 and T_3, T_3 and T_2, and T_2 and T_1, respectively.

For each wicking test run, the procedures were as follows: (1) positioned the sample 1–2 mm above the liquid surface; (2) calibrated the balance; (3) decreased the sample position 3 mm down into the liquid to start the wicking process; (4) lifted the sample 3 mm up out of the liquid after about 10 min. This would stop the wicking process and initiate the evaporation process; (5) kept recording the evaporation data until the sample weight was the same as at the beginning.

4. Results and discussion

The test matrix consists of two sample orientations and two initial temperature conditions. Three repeating runs were conducted for each condition, namely 12 measurements were performed in total. The initial temperature condition for each run is listed in Table 5.

For the high superheat condition, the temperature gradient was calculated from the slope of the temperatures of sensors T_{11}-T_{13}. The average superheat degree is about 25 K. For the low superheat condition, the gradient was calculated only from temperatures of T_{11}-T_{12} since the initial temperature of T_{13} had a big difference among different runs. The average superheat degree is below 2 K (exclude the part above T_{12}).

4.1. Mass and temperature developments during wicking test

Taking the test data of the warp sample as an example, the changes of mass and temperature over time are displayed in Fig. 9 for low superheat and in Fig. 10 for high superheat condition. The mass curves for both superheat conditions show a similar trend that a sharp increase occurs at first due to the wetting phenomenon which is also called Wilhelmy force [43]. Then, the mass begins to increase gradually through liquid wicking until it reaches a plateau due to the balance between capillary pressure and resistances of both gravity and evaporation. The following sharp mass drop indicates the sample was lifted up and lost the wetting meniscus. Finally, the mass gradually decreases to zero, representing the thorough evaporation of the residual liquid within the sample. There are also differences concerning wicking velocity and evaporation velocity between two cases, which will be further compared in Section 4.2.

Comparing the temperature changes of each sensor in Fig. 9, sensors T_1-T_7 almost keep constant below 79 K, providing a relative uniform and nearly isothermal cryogenic environment. The slight rise and fluctuation at the beginning and the end of the wicking process are mainly caused by the interference from sample moving and the thermal effect of illumination for visual operation. For

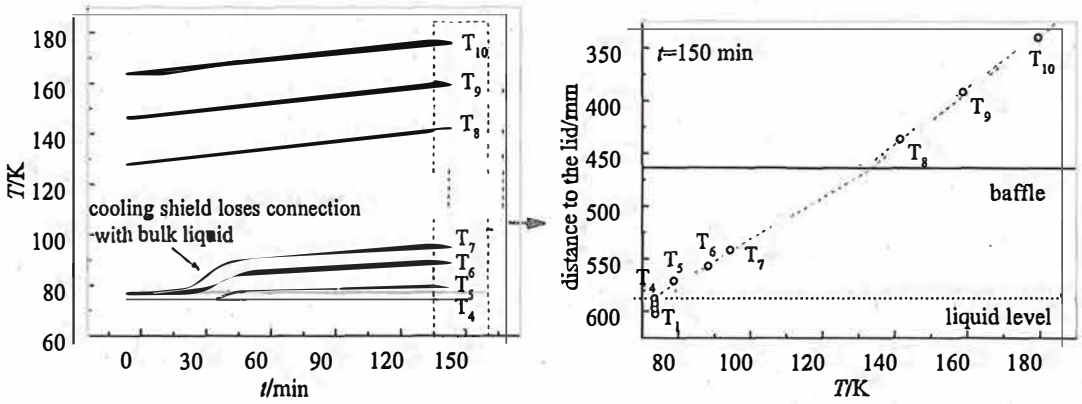

Fig. 8. Stable process for establishment of high superheat condition.

Table 5
Initial temperature condition for each case.

Items			T/K													∇T/K m^{-1}	Average linear ∇T/K m^{-1}
			T_1	T_2	T_3	T_4	T_5	T_6	T_7	T_8	T_9	T_{10}	T_{11}	T_{12}	T_{13}		
LSH	Warp	Run1	77.43	77.42	77.4	77.42	77.42	78.03	78.32	129.25	148.06	165.92	78.37	79.52	101.99	36.9	32.7 ± 3.8
		Run2	77.43	77.43	77.4	77.43	77.44	78.09	78.37	129.27	148.32	166.38	78.36	79.27	99.68	31.7	
		Run3	77.44	77.43	77.41	77.43	77.43	78.12	78.40	129.44	148.58	166.69	78.22	79.09	97.22	29.4	
	Shute	Run1	77.49	77.48	77.45	77.48	77.6	78.22	78.47	124.92	144.51	162.88	78.38	78.54	82.85	16.8	17.1± 1.3
		Run2	77.49	77.49	77.46	77.48	77.61	78.33	78.62	126.19	145.95	164.51	78.41	78.59	82.38	17.5	
		Run3	77.48	77.48	77.45	77.48	77.61	78.36	78.65	127.94	147.64	166.1	78.26	78.53	82.16	16.9	
HSH	Warp	Run1	77.46	77.45	77.44	77.97	83.06	92.86	99.42	146.17	163.35	179.75	88.40	102.16	116.57	483.5	491.5 ± 11.7
		Run2	77.45	77.45	78.22	79.73	85.94	95.75	102.42	150.81	167.61	183.74	88.82	102.74	117.29	486.1	
		Run3	77.44	78.22	79.93	81.76	90.53	98.75	105.56	154.16	170.89	186.95	90.18	104.39	118.80	504.9	
	Shute	Run1	77.43	77.42	77.40	77.98	83.02	92.64	98.97	145.27	162.42	178.73	87.46	100.77	114.74	466.6	471.3± 4.2
		Run2	77.43	77.44	78.34	79.86	86.09	95.79	102.24	149.52	166.14	182.00	88.82	102.45	116.45	474.8	
		Run3	77.44	78.37	80.00	81.75	89.99	98.24	104.66	152.11	168.65	184.46	88.63	102.34	116.00	472.5	

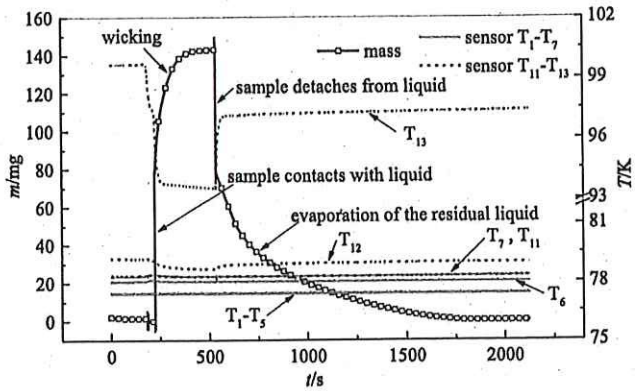

Fig. 9. Wicking process in warp direction under low superheat condition.

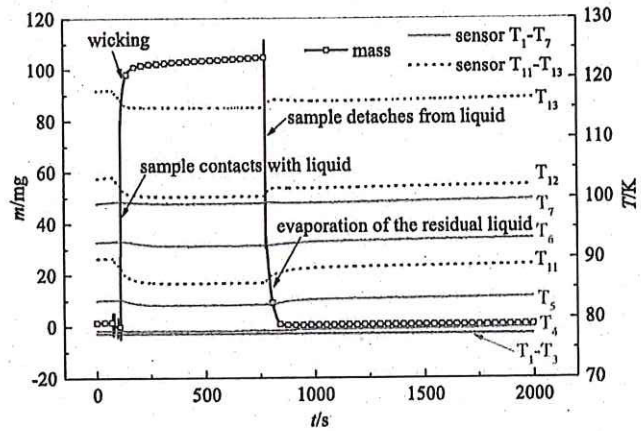

Fig. 10. Wicking process in warp direction under high superheat condition.

sensors T_{11}-T_{13}, which are synchronously moving with the sample, T_{11} is of the lowest temperature due to its lowest position close to the liquid level. Temperature of T_{13} is the highest, presenting an obvious change with its position and increasing the most after the wicking test. Sensor T_{13} is at the highest position among T_{11}-T_{13}, which is the closest to the baffle, hereby suffers the most severe thermal effect from above.

Different from Fig. 9, the temperature distribution in Fig. 10 presents a linear gradient along height for the high superheat case. Without the constant cooling from the wet porous shield, temperatures of all sensors keep increasing slightly after the wicking test. However, T_1-T_7 still have no marked change during test, implying the stratification of vapor environment would not be disturbed by the test operation. Besides, temperatures of T_{11}-T_{13} are stable during the wicking test but decrease with the sample descent and increase with the sample rise, similar to the trends of T_{12} and T_{13} in Fig. 9. It indicates that the temperatures of sensors on rod 2 are mainly determined by their positions in the stratification but barely influenced by the wicking process. In other words, the liquid wicking process within the sample cannot obviously disturb even the environment around the sample.

4.2. Effect of superheat degree

In order to visually compare the effect of the degree of superheat on the wicking performance, the development of the real wicking mass was extracted from the raw data of mass measurement (contains the disturbances of Wilhelmy force, immersion depth, et al.) using the data processing method introduced in Ref. [29]. As shown in Fig. 11, three repeating runs always have high coincidence for each condition, which indicates the good reproducibility of the experiment system and the reliability of the experiment results. It could be easily observed that, under high superheat condition, the mass increases more slowly and becomes stable at a lower value. The main reason is, under higher superheat condition, evaporation of the imbibed liquid in screen is more remarkable, resulting in a higher resistance to the wicking development. Finally, only a lower equivalent mass can be achieved based on the balance of the effects of capillary pressure, gravity and evaporation.

For a certain porous sample, the maximal mass of the accommodated liquid can be calculated by

$$m_{max} = \delta W H \phi \rho_l. \tag{19}$$

By substituting the related values (Tables 2–4) into Eq. (19), the maxima of the wicking mass are about 118.8 mg and 122.2 mg for warp and shute samples, respectively. From Fig. 11, at the LSH condition with a superheat degree of about 2 K, the equivalent wicking masses are around 73.1 mg and 78.5 mg for warp and shute samples, which are about 38.5% and 35.8% lower than the corresponding maximums. When the superheat degree increases to about 25 K, the equivalent wicking masses are about 31.7 mg and 26.6 mg for warp and shute samples, corresponding to a reduction of 73.3% and 78.2% from the maximums. This remarkable decreasing of the equivalent wicking mass as the increasing superheat could indicate the significant effect of the superheat condition on the wicking process.

The evaporation processes of each run in warp direction are shown in Fig. 12. The evaporation process in shute direction has a similar trend, therefore is not shown here. In order to unify the time deviation from three runs, a same mass of the residual liquid

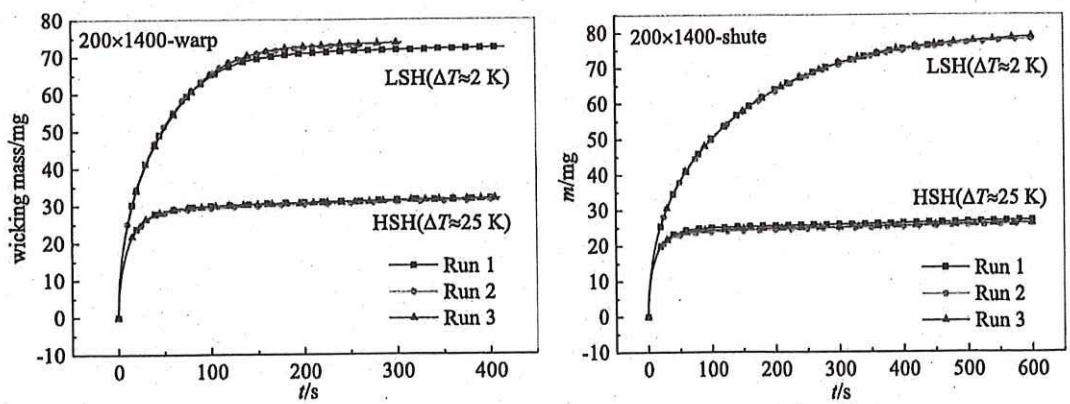

Fig. 11. Wicking mass development for each test run.

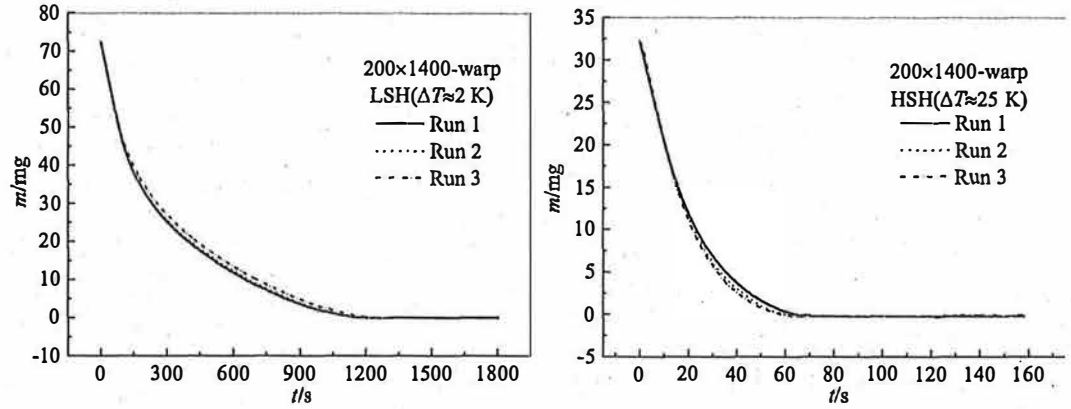

Fig. 12. Effect of superheat degree on evaporation rate.

is set as the starting point and the time axis is relocated for each case. It can be seen that, all curves have the concave shape indicating the decrease of the evaporation rate over time, which is mainly because the evaporation surface becomes smaller as the liquid evaporates. When the superheat degree increases from ~2 K to ~25 K, the average evaporation rate increases more than 10 times higher. The slight difference between each repeating run also obeys the same trend that the evaporation rate increases as the superheat degree.

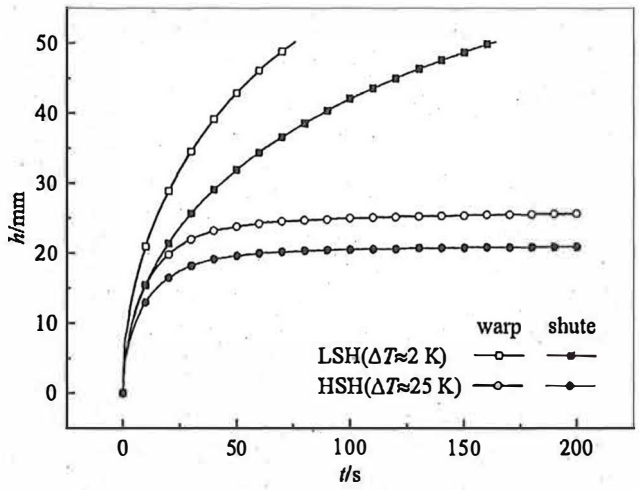

Fig. 13. Wicking height developments for each test condition.

4.3. Effect of wicking direction

Fig. 13 displays the average results of the wicking height versus time for each condition. The wicking height was calculated from the data of mass change as

$$h(t) = \frac{m(t)}{\delta W \phi \rho_l}, \tag{20}$$

where the maximal wicking height should be the height of the sample (H in Table 2). It should be noted that only the data of wicking height below T_{12} were used for comparison, since the initial temperature of T_{13} had a big difference among different runs (Table 5) for the low superheat condition, It could be revealed from Fig. 13 that, the wicking height always increases faster in the warp direction than that in the shute direction for two superheat conditions. A higher wicking velocity usually corresponds to a better performance, since the faster the wicking velocity is, the faster the channel of LAD could start to play a role of gas blocking, also the faster the screen could recover the function after breakdown [10]. However, some researchers also claimed that, high wicking rates might be undesirable for LAD filling or refilling since the wicking might seal the device prematurely and fail to clear the gas for gas free liquid delivery [26].

4.4. Comparison with theoretical model

According to the conditions and results of experiment, a comparative calculation was also performed to evaluate the modified theoretical model proposed in Section 2. As essential inputs, macroscopic parameters including porosity, equivalent capillary diameter and permeability were set at the values listed in Table 3.

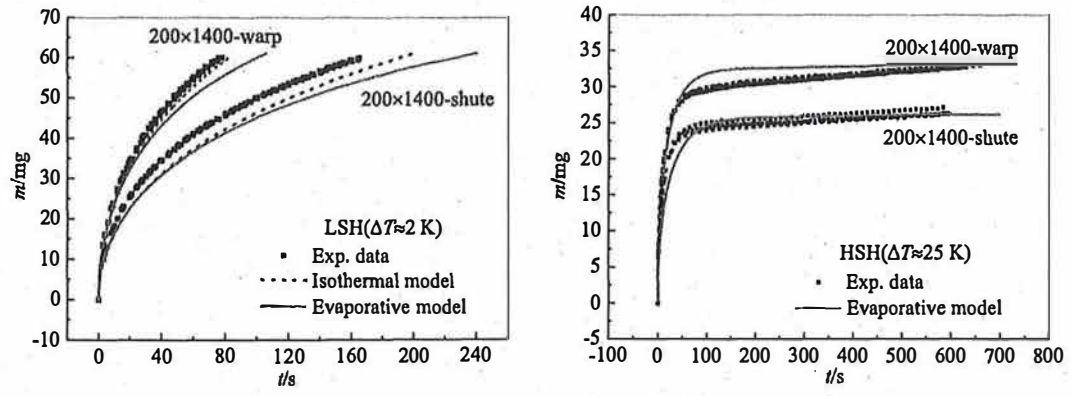

Fig. 14. Comparison between experimental data and theoretical predictions.

The average temperature gradients in Table 5 were used as input for the initial superheat condition.

As the comparative results shown in Fig. 14, the calculating curves for all cases present a fair agreement with the experiment data, verifying the reasonability of the wicking theory used in this paper. For low superheat condition, predictions by the isothermal model in Eq. (2) are also displayed for comparison, which are higher than the results of the non-isothermal model but still underestimate the experiment data. Similar results also have been obtained by Grebenyuk et al. [37]. A probable reason for this deviation between calculated and experimental results is speculated to be the error propagation from experiment measurement and the post processing of data. Besides, there is also a possibility that the macroscopic parameters of the porous structure might have unpredictable deviations under different temperatures. However, the exact reason is difficult to determine from the current results and further investigation is needed.

By contrast, the prediction for high superheat condition has a better goodness of fit than that under low superheat condition. Although some errors occur at the early stage, the equilibrium mass at the final stage could be predicted with high accuracy. The information of the relative error for each case is listed in Table 6.

Taking the data of the warp sample as an example (similar results for shute sample), Fig. 15 illustrates the predicted heat transfer rates from screen solid and gas regions under LSH and HSH conditions, respectively. It can be easily discovered that, at LSH condition, the heat transfer intensity is overall much lower than that at HSH. However, the heat transfer rates from solid and gas region show a similar change rule under the two superheated conditions.

Since the initial value of $\dot{q}_{sl}$ is set as zero and the wicking velocity is very fast at the very beginning, $\dot{q}_{sl}$ presents a wave peak during the first few time steps. After that, $\dot{q}_{sl}$ gradually decreases along the wicking process and becomes zero after the wicking height achieving equilibrium, which is similar to the change of wicking velocity. This can be verified by Eq. (7) that, $\dot{q}_{sl}$ is in direct proportion to the evaporative wicking velocity u_e.

Table 6
Relative errors of the theoretical results compared to experiment data.

Condition	Model	Relative error/%			
		Warp		Shute	
		Max.	Average	Max.	Average
LSH	Isothermal	14.83	3.65	17.8	7.74
	Evaporative	13.79	6.86	15.6	10.1
HSH	Evaporative	26.29	4.12	9.68	3.32

Meanwhile, the heat transfer intensity of natural convection between gas and wet screen presents a similar trend with the wicking height. The reason is, on the one hand, as the wicking height increases, the surface area of the wet screen part increases and the average temperature difference increases as well due to the linear distribution of the superheat environment. On the other hand, referring to Eq. (11), Gr also increases based on a larger characteristic length l and a larger temperature difference. Therefore, according to Eqs. (9)–(11), $\dot{q}_{gl}$ has a positive correlation with the wicking height development. When the wicking process finally reaches an equivalent state, Gr, heat transfer area and temperature difference also stabilize at a certain value, resulting in a constant $\dot{q}_{gl}$ as shown in Fig. 15.

As for the integral heat transfer rate, early in the wicking process, it depends on the combined actions of heat transfer from solid and gas. Then, as the increase of $\dot{q}_{gl}$ and the decrease of $\dot{q}_{sl}$, the duty of $\dot{q}_{gl}$ is growing. Finally, after the wicking process reaches equilibrium, the total heat transfer rate is only determined by $\dot{q}_{gl}$. This indicates that, for the thin screens studied in this paper, the thermal effects of solid and gas regions both play a very important role and must be considered during superheated wicking processes.

On the whole, with an acceptable average relative error below 10%, the modified model is considered reasonable and reliable to predict the superheated wicking process. Hereby, in view of the difficulty and cost for experimental measurement, the theoretical model is recommended as an efficient tool when all of the necessary information for model calculation are given.

5. Conclusions

As an important feature for liquid channel LADs, the wicking performance in metallic screens is theoretically and experimentally investigated in this paper. Main conclusions are listed as follows:

(1) Cryo-wicking of LN_2 in DTW 200 × 1400 was measured under two superheat degrees (~2 K and ~25 K) and in both warp and shute directions, which could effectively supplement the lack of data at cryogenic temperature. In the open literatures, this is the first time to obtain available data of cryo-wicking at nearly isothermal condition.

(2) The vertical cryo-wicking process also obey the basic wicking mechanism that, the wicking height increases faster at the beginning then slows down and finally stabilizes at a maximum reachable height. At the same superheat condition, the wicking velocity is always higher in warp direction, consistent with the findings from other experiments [25,26,28,29].

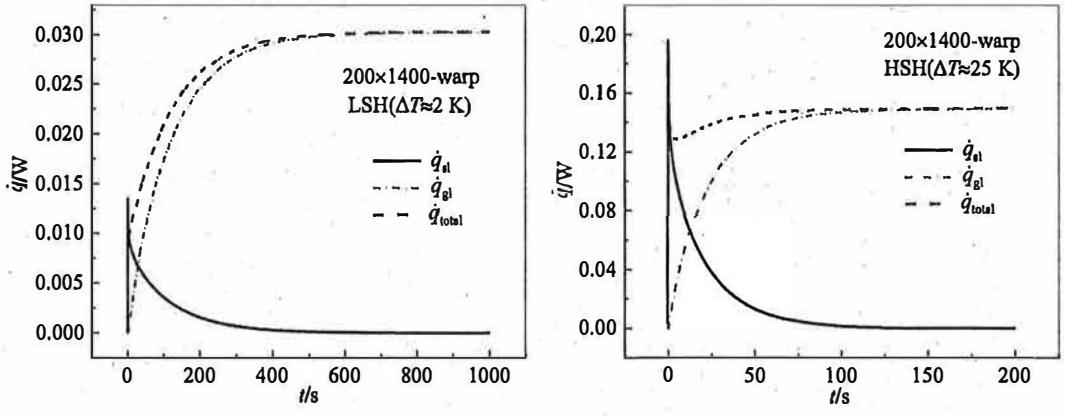

Fig. 15. Thermal effects of screen solid and gas region during wicking process.

(3) The wicking process in thin metallic screen is weak and sensible, which almost has no thermal effect on the surrounding environment but was remarkably influenced by the superheat condition of surroundings. Under a higher superheat condition, the wicking process obviously slows down and the reachable wicking height is much lower.
(4) Based on the isothermal porous-continuum model, a modified evaporative wicking model was proposed by taking the evaporation effect caused by both superheated porous media and atmosphere into account. With an acceptable average error below 10% compared to the experiment data, this model was verified to be effective and reasonable for prediction of the superheated wicking process of cryogenic liquids within metallic screens.

Declaration of Competing Interest

The authors declared that there is no conflict of interest.

Acknowledgements

This work was supported by the National Natural Science Foundation of China (51876153) and the Research Fund of State Key Laboratory of Technologies in Space Cryogenic Propellants (SKLTSCP1810). The first author is grateful to the China Scholarship Council (CSC) for funding her oversea study. D.Z. and M.D. acknowledge the support from the Deutsche Forschungsgemeinschaft (DFG) research training group MIMENIMA (GRK 1860) and technical assistance from Peter Prengel and Frank Ciecior.

References

[1] E. Slachmuylders, W. Berry, D.N. Soo, C. Savage, Fluid dynamic problems in space systems, ESA Proceedings of an International Symposium on Fluid Dynamics and Space (1986) 65–82.
[2] R.N. Eberhardt, T.R. Tracey, W.J. Bailey, Orbital spacecraft resupply technology, AIAA 86-1604, 1986.
[3] Y. Ma, Y. Li, K. Zhu, Y. Wang, L. Wang, Investigation on no-vent filling process of liquid hydrogen tank under microgravity condition, Int. J. Hydrogen Energy 42 (12) (2017) 8264–8277.
[4] J. Aydelott, J. Gille, R. Eberhardt, On-orbit cryogenic fluid transfer, AIAA 84-1343, 1984.
[5] E.C. Cady, R.R. Corban, S.M. Stevenson, Cryogenic propellant management architectures to support the Space Exploration, AIAA 90-3713, 1990.
[6] D. Chato, Cryogenic transfer options for exploration missions, AIAA 91-3541, 1991.
[7] D.L. Balzer, Y. Brill, R.K. Grove, R.O. Sloma, A survey of current developments in surface tension devices for propellant acquisition, J. Spacecraft Rockets 8 (2) (1971) 83–98.
[8] D.A. Fester, A.J. Villars, P.E. Uney, Surface tension propellant acquisition system technology for Space Shuttle Reaction Control Tanks, J. Spacecraft Rockets 13 (9) (2012) 522–527.
[9] J.R. Tegart, S.L. Driscoll, L.J. Hastings, Fluid acquisition and resupply experiments on space shuttle flights STS-53 and STS-57, Marshall Space Flight Center, Alabama, USA, NASA/TP-2011-216465, April 2011.
[10] J. Hartwig, J. Mcquillen, Performance gains of propellant management devices for liquid hydrogen depots, NASA/TM—2013-217834, AIAA-2013-0368, 2013.
[11] S. Darr, J. Hartwig, Optimal liquid acquisition device screen weave for a liquid hydrogen fuel depot, Int. J. Hydrogen Energy 39 (9) (2014) 4356–4366.
[12] M. Conrath, M. Dreyer, Gas breakthrough at a porous screen, Int. J. Multiph. Flow 42 (2012) 29–41.
[13] J. Hartwig, D. Chato, J. Mcquillen, Screen channel LAD bubble point tests in liquid hydrogen, Int. J. Hydrogen Energy 39 (2) (2014) 853–861.
[14] A.J. Savas, J.W. Hartwig, J.P. Moder, Thermal analysis of a cryogenic liquid acquisition device under autogenous and non-condensable pressurization schemes, Int. J. Heat Mass Transf. 74 (5) (2014) 403–413.
[15] J. Hartwig, J.A. Mann, A predictive bubble point pressure model for porous liquid acquisition device screens, J. Porous Med. 17 (17) (2014) 587–600.
[16] J.W. Hartwig, Y. Kamotani, The static bubble point pressure model for cryogenic screen channel liquid acquisition devices, Int. J. Heat Mass Transf. 101 (2016) 502–516.
[17] J.W. Hartwig, Screen channel liquid acquisition device bubble point tests in liquid nitrogen, Cryogenics 74 (2016) 95–105.
[18] J.W. Hartwig, S.R. Darr, J.B. Mcquillen, E. Rame, D.J. Chato, A steady state pressure drop model for screen channel liquid acquisition devices, Cryogenics 64 (2014) 260–271.
[19] J.B. Mcquillen, D.J. Chato, B.J. Motil, M.P. Doherty, D.F. Chao, N.L. Zhang, Porous screen applied in liquid acquisition device channel and CFD simulation of flow in the channel, J. Porous Med. 15 (5) (2012) 429–437.
[20] J.W. Hartwig, D.J. Chato, J.B. Mcquillen, J. Vera, M.T. Kudlac, F.D. Quinn, Screen channel liquid acquisition device outflow tests in liquid hydrogen, Cryogenics 64 (2014) 295–306.
[21] S.R. Darr, C.F. Camarotti, J.W. Hartwig, J.N. Chung, Hydrodynamic model of screen channel liquid acquisition devices for in-space cryogenic propellant management, Phys. Fluids 29 (1) (2017) 017101.
[22] J.W. Hartwig, Y. Kamotani, The static reseal pressure model for cryogenic screen channel liquid acquisition devices, Int. J. Heat Mass Transf. 99 (2016) 31–43.
[23] N. Fries, K. Odic, M. Conrath, M. Dreyer, The effect of evaporation on the wicking of liquids into a metallic weave, J. Colloid Interface Sci. 321 (1) (2008) 118.
[24] M. Zhang, Capillary Transport of Cryogenic Liquids in Porous Media. Doctoral dissertation, Cuvillier Verlag, Göttingen, 2013.
[25] E.P. Symons, Wicking of Liquids in Screens, NASA TN D-7657, 1974.
[26] F.T. Dodge, The new "dynamic behavior of liquids in moving containers", Southwest Research Inst., San Antonio, TX, 2000.
[27] M. Conrath, Y. Smiyukha, E. Fuhrmann, M. Dreyer, Double porous screen element for gas-liquid phase separation, Int. J. Multiph. Flow 50 (4) (2013) 1–15.
[28] J. Hartwig, S. Darr, Influential factors for liquid acquisition device screen selection for cryogenic propulsion systems, Appl. Therm. Eng. 66 (1) (2014) 548–562.
[29] Y. Ma, Y.Z. Li, L. Wang, G. Lei, T.X. Wang, Investigation on isothermal wicking performance within metallic weaves for screen channel liquid acquisition devices (LADs), Int. J. Heat Mass Transf. 135 (2019) 392–402.
[30] M. Conrath, N. Fries, M. Zhang, M. Dreyer, Radial capillary transport from an infinite reservoir, Transp. Porous Med. 84 (1) (2010) 109–132.
[31] H. Zhang, Q. Pan, H. Zhang, Multi-scale porous copper foams as wick structures, Mater. Lett. 106 (9) (2013) 360–362.
[32] M.R.S. Shirazy, L.G. Fréchette, Capillary and wetting properties of copper metal foams in the presence of evaporation and sintered walls, Int. J. Heat Mass Transf. 58 (1–2) (2013) 282–291.
[33] Z. Liu, J. Hu, Y.M. Zhao, Z.G. Qu, F. Xu, Experimental and numerical studies on liquid wicking into filter papers for paper-based diagnostics, Appl. Therm. Eng. 88 (2015) 280–287.
[34] L.J. Hastings, L.G. Bolshinskiy, R.G. Schunk, A.K. Martin, R.H. Eskridge, B.D. Hamill, C.F. Gomez, A. Frenkel, G. Grayson, M.L. Pendleton, Thermal integration of a liquid acquisition device into a cryogenic feed system, Marshall Space Flight Center, USA, NASA/TP-2011-216474, 2011.
[35] T. Zhang, P. DeBock, E.W. Stautner, T. Deng, C. Immer, Demonstration of liquid nitrogen wicking using a multi-layer metallic wire cloth laminate, Cryogenics 52 (4–6) (2012) 301–305.
[36] S.W. Choi, W.I. Lee, H.S. Kim, Analysis of flow characteristics of cryogenic liquid in porous media, Int. J. Heat Mass Transf. 87 (2015) 161–183.
[37] Y. Grebenyuk, M.E. Dreyer, Wicking of liquid nitrogen into superheated porous structures, Cryogenics 78 (2016) 27–39.
[38] R. Masoodi, K.M. Pillai, Wicking in Porous Materials: Traditional and Modern Modeling Approaches, CRC Press, 2012, Chapter 3–5: 31–131.
[39] F.A.L. Dullien, Porous Media: Fluid Transport and Pore Structure, Academic press, 2012, Chapter 1: 6-20.
[40] J.P. Holman, Heat Transfer, Osborne McGraw-Hill, 1985.
[41] S.M. Yang, Z.Z. Zhang, An experimental study of natural convection heat transfer from a horizontal cylinder in high Rayleigh number laminar and turbulent regions, Proceedings of the 10th International Heat Transfer Conference, Brighton, vol. 7, 1994, pp. 185–189.
[42] R. Karwa, Empirical Relations for Natural or Free Convection, Heat and Mass Transfer, Springer, Singapore, 2017.
[43] A. Al-Shareef, P. Neogi, B. Bai, Force based dynamic contact angles and wetting kinetics on a Wilhelmy plate, Chem. Eng. Sci. 99 (32) (2013) 113–117.